Nuclear Materials and Energy 28 (2021) 101028

Contents lists available at ScienceDirect

Nuclear Materials and Energy

journal homepage: www.elsevier.com/locate/nme

High-dose ion irradiation damage in $Fe_{28}Ni_{28}Mn_{26}Cr_{18}$ characterised by TEM and depth-sensing nanoindentation

A. Fernández-Caballero [a,b,c,*], E. Bousser [d,g], S.M. Shubeita [e], P.T. Wady [e], Y. Gu [g,f], Ram Krishna [g], M.J. Gorley [b], D. Nguyen-Manh [b], P.M. Mummery [c], E.J. Pickering [g]

[a] Department of Engineering Science, University of Oxford, Parks Road, Oxford, OX1 3PJ, UK
[b] CCFE, United Kingdom Atomic Energy Authority, Abingdon OX14 3DB, UK
[c] Department of Mechanical Aerospace and Civil Engineering, University of Manchester, Manchester M13 9PL, UK
[d] Engineering Physics Department, École Polytechnique de Montréal, P.O. Box 6079, Station Centre-ville, Montréal, Québec H3C 3A7, Canada
[e] Dalton Cumbrian Facility, The University of Manchester, Moor Row CA24 3HA, UK
[f] Swansea University Bay Campus College of Engineering, Crymlyn Burrows, Swansea, SA1 8EN, UK
[g] Department of Materials, University of Manchester, Manchester M13 9PL, UK

ARTICLE INFO

Keywords:
High-entropy alloy
Multicomponent alloy
Irradiation
Dislocation loops
TEM
STEM–EDX
XRD
Hardness
Depth-sensing nanoindentation

ABSTRACT

One of the key challenges for the development of high-performance fusion materials is to design materials capable of maintaining mechanical and structural integrity under the extreme levels of displacement damage, high temperature and transmutation rates. High-entropy alloys (HEAs) and other concentrated alloys have attracted attention with regards to their performance under fusion conditions. In recent years, a number of investigations of the irradiation responses of HEAs have peaked the community's interest in them, such as the work of Kumar et al. (2016), who examined $Fe_{27}Ni_{28}Mn_{27}Cr_{18}$ at doses as high as 10 dpa. In this work, we study $Fe_{28}Ni_{28}Mn_{26}Cr_{18}$ concentrated multicomponent alloy with irradiation doses as high as 20 dpa. We find the presence of Cr rich bcc precipitates in both the un-irradiated and in the irradiated condition, and the presence of dislocation loops only in the irradiated state. We correlate the features found with irradiation hardening by the continuous stiffness method (CSM) depth-sensing nanoindentation technique and see that the change in the bulk hardness increases significantly at 20 dpa for temperatures 450 °C. These results indicate that the alloy is neither stable as a single phase after annealing at 900 °C, nor particularly resistant to irradiation hardening.

1. Introduction

Alloys containing five or more elements in nearly equal atomic concentration or with more than 5% concentration have been referred as high entropy alloys after Yeh at al. [1,2] or as multi-component alloys (MCPs) after Cantor et al. [3]. The high number of different combinations of elements in concentrated multicomponent alloys can make possible the discovery of materials properties that cannot be achieved in conventional alloys, which typically contain one principal element. The interest of concentrated multicomponent alloys as high-temperature structural materials for nuclear industries has been motivated by some reports of attractive mechanical properties at elevated temperatures including hardness, strength, ductility, wear, and radiation and corrosion resistance [4].

The structural materials for fusion reactors plants will experience very demanding environments in terms of high temperatures (300–800 °C) and intense 14 MeV neutron irradiation fluxes [5] posing potential challenges to mechanical strength, fracture toughness and ductility and dimensional changes due to void swelling and creep [6]. The development of high-performance materials that are radiation resistant is critical for advanced nuclear reactor systems. Due to their chemical complexity, different atomic sizes and charge transfer among the elements in the random solid solution of concentrated multicomponent alloys, atomic-level stresses have been rationalised as the cause for reduced number densities of vacancy or interstitial defect clusters due to enhanced vacancy-interstitial recombination of defect clusters in the cascade following the thermal spike after irradiation by high energy particles [7–10].

* Corresponding author at: Department of Engineering Science, University of Oxford, Parks Road, Oxford, OX1 3PJ, UK.
E-mail addresses: antonio.fernandez-caballero@eng.ox.ac.uk, antoniferca@icloud.com (A. Fernández-Caballero).

https://doi.org/10.1016/j.nme.2021.101028
Received 31 January 2021; Received in revised form 9 May 2021; Accepted 17 May 2021
Available online 21 May 2021

Recently, attention has been drawn to concentrated multicomponent alloys, in particular, containing light transition metal elements Co, Cr, Fe, Ni, and Mn that form predominantly a single phase with secondary phase precipitates after prolonged heat treatments [3,11]. For some of the alloys belonging to the family of CrMnFeCoNi but without Co, mechanical tensile tests have indicated that these alloys can become brittle due to the presence of the hard and brittle σ phase [11, 12]. The embrittlement studies motivated the study of particular alloy compositions, specifically Cr content controlled to narrow down selection to composition $Fe_{28}Ni_{28}Mn_{26}Cr_{18}$ [13]. The composition of $Fe_{28}Ni_{28}Mn_{26}Cr_{18}$ is also favoured for nuclear applications due to the removal of Co. If Co is exposed to intense high energy neutron fluxes, it can transmute into ^{60}Co long-lived radioactive isotope [14].

In previous work [15], the microstructure and hardness of 5.8 MeV ion irradiated $Fe_{27}Ni_{28}Mn_{27}Cr_{18}$ concentrated multicomponent alloy was studied up to doses of 10 dpa and temperatures of 700 °C by TEM and by depth-sensing nanoindentation. In the study, the concentrated multicomponent alloy was reported to be a single-phase solid solution and remain stable during irradiation. The essential radiation-induced features were high density dislocation loops, reduced grain boundary Cr and Fe and increased Ni segregation compared to FeCrNi austenitic stainless steels irradiated to similar doses, and lack of void formation. The authors rationalised the small size, and high number density of dislocation loops in comparison to equivalent irradiated FeCrNi austenitic stainless steels as being due to a reduced point defect recombination in this concentrated multicomponent alloy.

Heavy-ion irradiations have been used as simulation experiments for neutron damage in structural materials since they are amenable to flexible environmental conditions, including control of temperature and displacement per atom rate [16]. These parameters are not so easily controlled during in-reactor irradiation experiments. Furthermore, the high rates of displacement per atom from heavy ion irradiations, which are several orders of magnitude higher than for neutron irradiation, speed up the accumulation of radiation damage [16]. The drawbacks of heavy ion irradiation are mainly the few μm ranges of implanted damage depth that makes difficult sample preparation for microscopy.

This work aims to assess the irradiation behaviour of the $Fe_{28}Ni_{28}Mn_{26}Cr_{18}$ alloy in detail at high doses to further confirm the apparent irradiation resistance of the alloy. In Section 2 the experimental methods for the thermomechanical processing of the sample preparation, the self-ion irradiation, the depth-sensing nanoindentation and TEM sample preparation are described; In Section 3 the microstructure of $Fe_{28}Ni_{28}Mn_{26}Cr_{18}$ is characterised in un-irradiated state by TEM, then the microstructure of the 5 MeV Ni irradiated $Fe_{28}Ni_{28}Mn_{26}Cr_{18}$ is characterised by TEM, and then hardening is studied from depth-sensing nanoindentation measurements.

2. Experimental methods

2.1. Thermo-mechanical processing and sample preparation

The $Fe_{28}Ni_{28}Mn_{26}Cr_{18}$ concentrated multicomponent alloy specimens were prepared by arc melting in a Ti-gettered high-purity argon atmosphere by mixing high purity (99.9%) elemental Cr, Mn, Fe and Ni in the concentration of 18%–27%–27%–28% at.% respectively. The ingots were flipped and remelted several times during the arc melting process.[1] To cross-check the average chemical composition of the as-cast concentrated multicomponent alloys analysis with a FEI Quanta 650 SEM (Scanning Electron Microscope) Oxford instruments EDX (Energy Dispersive X-rays) was conducted over 10 regions of approximate area of 100 μm by 100 μm. The resulting analysis is shown in Table 1, which agrees reasonably well with the expected composition values, thus indicating that no relative depletion of any alloy element in the bulk occurred in the manufacturing process.

[1] The samples were prepared at the University of Sheffield within Accelerated Metallurgy project.

Table 1
Chemical composition of $Fe_{28}Ni_{28}Mn_{26}Cr_{18}$ concentrated multicomponent alloys for this work, measured with SEM–EDX.

Element	wt.% [15]	wt.% (this work)	at.% (this work)
Cr	18	16.7 ± 0.3	18.0 ± 0.1
Mn	27	25.6 ± 0.6	26.0 ± 0.6
Fe	27	28.1 ± 0.5	28.1 ± 0.3
Ni	28	29.3 ± 0.5	27.9 ± 0.3

More detailed analysis performed with EDX revealed micro-segregation at the μm scale with the presence of dendrite-like structures of approximately 20 μm spacing see Figs. 1(a)–(d). To homogenise and anneal possible sinks for irradiation defects in the microstructure we performed a homogenisation heat treatment at 1200 °C for 48 h and water quench, then deformed in an uniaxial compression to a thickness reduction of 40%. And finally a re-crystallisation heat treatment at 900 °C for 4 h followed by furnace cooling. The results are shown in Figs. 1(e)–(h). The heat treatment was performed to reproduce work by Kumar et al. [15].

Thermomechanically processed specimens were electro-discharge machined into square blocks of approximate size 10 mm and thickness between 0.5 and 1 mm. Grinding was performed with SiC paper P800, P1200, P2400 and P4000, then followed by polishing with 1 μm polycrystalline diamond suspension in a cloth, and finally the specimens were OPS polished until grain boundaries appeared slightly etched in the optical microscope Zeiss Axio. The mean grain size in the recrystallised condition was found to be approximately 31 ± 9 μm by using a simple linear intercept method from the SEM micrograph in Fig. 2.

The recrystallised condition was characterised by X-ray diffraction (XRD) shown in Fig. 2 to ascertain that the crystal structure is face-centred cubic (fcc) and to find the lattice spacing. The powder diffractometer used for this work was a Phillips XRD PANalytical X'Pert Pro using a combined characteristic radiation of CuKα_1 and CuKα_2 X-rays with a Ni foil to remove β X-ray radiation and a graphite monochromator to reduce fluorescence effects that can mask the diffraction peaks in samples containing transition metal elements (our sample has Fe, Cr, Mn and Ni). This diffractometer used the $\theta - 2\theta$ Bragg–Brentano geometry, and the sample was spun along the normal to its planar surface. The working voltage of the diffractometer was 40 kV, and the operating current was 40 mA. The scanning region ranged from 35° to 110°, in steps of 0.05°.

We use the CMPR software [17] to investigate the parameters of the structure by predicting the angular location for the diffracted intensities from basic crystallographic information and optimise the lattice constants to fit the experimental intensity peak positions.

2.2. Self-ion irradiation experiment

For the irradiation experiment, the recrystallised specimens were mounted on the sample end-stage at the 30° beamline from Dalton Cumbrian Facility [18]. The beam was focused and operated in rastering mode. The last beam slits were adjusted to trim the beam to irradiate an area uniformly of 7 by 7 mm^2 area for all of the samples reported in this study. The sample temperature was monitored continuously throughout the irradiation experiment by thermal imaging to measure the temperature increase due to the combined beam heating and external heaters (see Fig. 3). The real beam current on the sample was monitored through the continuous reading of charge deposited at the end-stage by a data acquisition system implemented with LabView National Instruments. Corrections were applied to the measured beam current on the sample to compensate for the spurious secondary electron emission after the impact of heavy ions on the surface.

The displacements per atom (dpa) were estimated from SRIM (2008 version) [19] code and at 80% depth of the Bragg peak for 5 MeV

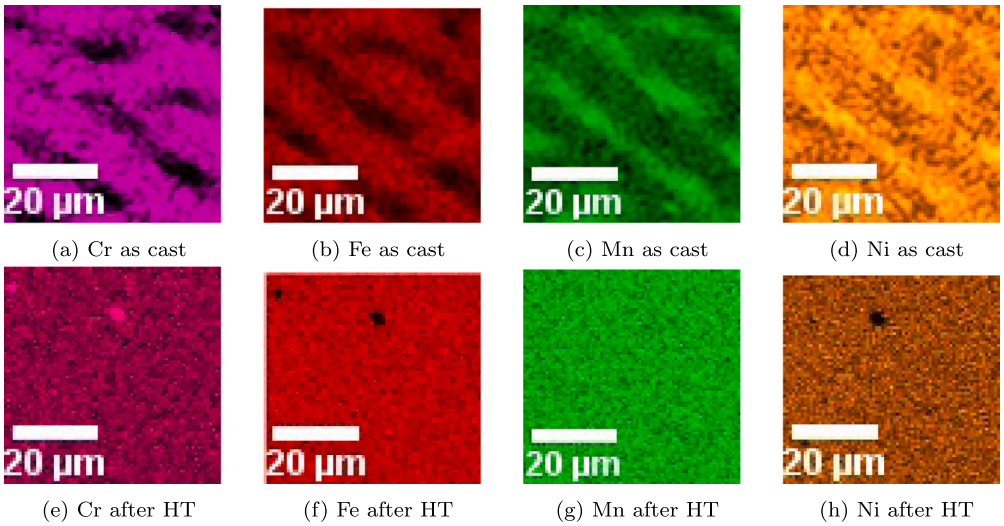

Fig. 1. Representative SEM–EDX maps of Cr, Fe, Mn and Ni before a–d and after e–h homogenisation heat treatment in as cast $Fe_{28}Ni_{28}Mn_{26}Cr_{18}$ concentrated multicomponent alloys at 1200 °C for 48 h. During the homogenisation and recrystallisation heat treatments MnCr oxide inclusions appeared, these are shown in the heat treated maps as black dots.

Table 2
Irradiations performed at Dalton Cumbrian Facility [18] with Nickel ions (excitation state +3) at 5 MeV under different conditions. The dose rate (dpa/s) was 2.4E−04 for all but the 2nd sample in the Table for which was 4.40E−04.

Ion fluence (ion/cm^2)	Dose (dpa)	Temperature (°C)	Exposure (time)
8.00E+14	2	300	2 h 19 min
8.00E+15	20	300	12 h 37 min
8.00E+15	20	450	23 h 9 min
8.00E+14	2	450	2 h 19 min
8.00E+13	0.2	450	0 h 14 min

Ni ions with +3 charge state. To make consistent our ion irradiation doses with potential future neutron irradiations we set up the SRIM simulation with lattice and surface binding energies of the Cr, Mn, Fe and Ni atoms equal to zero and we choose the Kinchin–Pease calculation mode following findings from [20]. For the displacement energies of the lattice atoms Cr, Fe, Mn and Ni the value 40 eV was used [20]. The peak dpa is estimated from SRIM dpa per fluence and the estimated fluence of the ion irradiation deposited charge corrected on each of our specimens (see Fig. 3).

The peak dose achieved was approximately 20 dpa, and the peak Ni implantation was approximately 0.14 at.%, as indicated in Figs. 3 (a), and 3 (b) respectively. The values for the main parameters fluence, dose, irradiation temperature, exposure time and dose are detailed in Table 2.

2.3. Depth-sensing nanoindentation methods

For carrying out depth-sensing nanoindentation, we used an MTS Nano Indenter XP equipped with a Berkovich geometry diamond indenter. The maximum allowed drift rate was set to 0.15 nm/s and a surface approach velocity for the tip of 10 nm/s. The penetration depth examined in the irradiated specimens ranged from 0 to 2000 nm with a maximum load of 200 mN. The projected contact area of the tip was evaluated using a fused silica standard material with E_r=69.6 GPa (reduced modulus) and ν=0.17 (Poisson's ratio) over a contact depth range from approximately 5 to 1400 nm. The average hardness values were determined from averaging 25 hardness values each being derived from a continuous load–displacement curve by using the continuous stiffness method (CSM) using the approach proposed by Oliver and Pharr [21]. The 25 (5 × 5) impressions were spread in an array of points separated by 50 μm to avoid interference effects due to localised plastic zones among the indents (see Fig. 2).

2.4. TEM sample preparation

TEM lamellae for characterising the 1 μm thin irradiated layer were prepared by the FIB lift-out method using Ga ions in an FEI Quanta 3D operated at 30 kV. Final cleaning–polishing was performed at 2 kV to minimise Ga ions induced damage on the microstructure until lamellae were electron transparent. The lamellae were mounted in a Cu TEM grid. The lamellae were observed in Tecnai F20, and an FEI Talos F200 A with TEM and STEM–EDX modes both operated at the accelerating voltage of 200 kV. The scale bar for diffraction was calibrated by using the fitted lattice spacing for fcc structure of the recrystallised condition in the powder diffraction measurements. The statistics of dislocation loop size and area density were obtained from TEM micrographs and analysed using Fiji (ImageJ) band-pass filter and threshold algorithms [22].

3. Results and discussion

3.1. Microstructural characterisation in the un-irradiated condition

The XRD pattern from the recrystallised microstructure indicates that the fcc structure is the main phase within the detection limits of the signal-to-noise ratio (Fig. 2). The single-phase stability of $Fe_{28}Ni_{28}Mn_{26}Cr_{18}$ concentrated multicomponent alloys is in agreement with the chemical homogeneity colour maps of Cr, Mn, Fe and Ni in the SEM–EDX results after annealing (see Fig. 1). The lattice parameter was found to be 3.610 ± 0.005 Å in space group O_h^5, this corresponds to the stress free microstructure. A lattice parameter of 3.64 Å was found from the alloy of Cr, Mn, Fe and Ni with similar composition in the fcc phase [15]. The relative height of the diffracted intensities is different from that expected by the intrinsic lattice geometrical multiplicities of a randomly oriented aggregate of crystals as typically used in conventional powder diffraction. This is likely to be an indicator of some crystallographic texture resulting from the thermomechanical processing applied.

SEM–EDX maps (shown in Fig. 1) and TEM selected area diffraction from the matrix (Fig. 4(a)) material confirmed the XRD predictions of fcc homogeneous solid solution phase except for oxide inclusions abundant in Mn and Cr associated to the spinel structure. Their presence could be related to the oxygen impurities in the raw materials or contamination in the manufacturing process in the arc melter. Similar inclusions have been found for Cantor alloy [11,23].

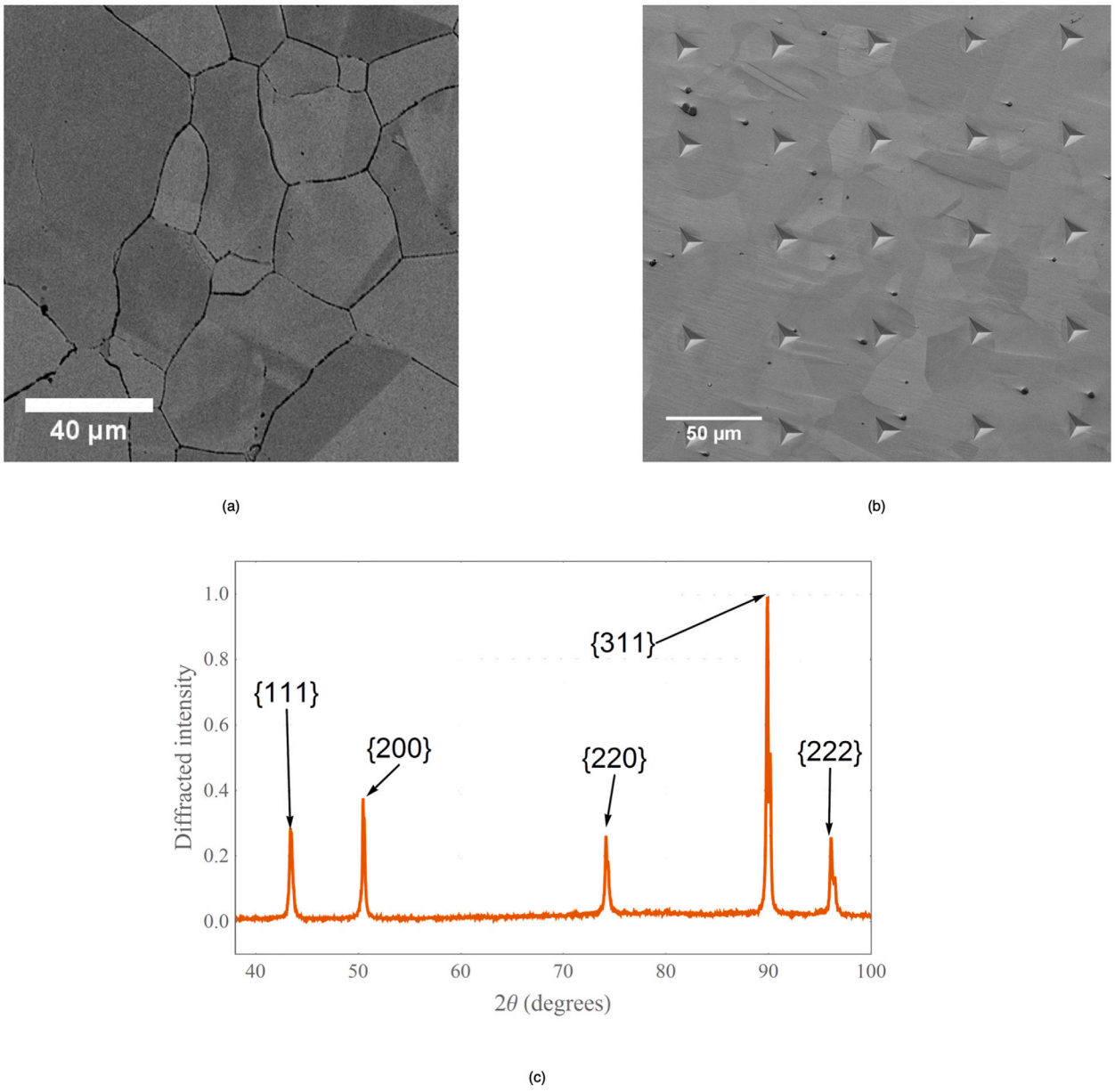

Fig. 2. (a) SEM Backscattered electron micrograph of the recrystallised microstructure indicating the grain structure after etching with metallographic etchant of nitric acid and ethanol. (b) Representative SEM image of array depth-sensing nanoindentation impressions after testing. The impressions are spaced approximately 50 µm apart and were performed on a sample irradiated at 300 °C and 20 dpa. (c) XRD diffraction pattern as obtained from recrystallised $Fe_{28}Ni_{28}Mn_{26}Cr_{18}$ concentrated multicomponent alloy. The secondary peaks to the right of the highest peaks are due to diffraction caused by longer wavelength of $CuK\alpha_2$ radiation.

TEM of the recystallised alloy revealed precipitates at the grain boundaries. By calculating the distance between diffraction spots along with the (200) directions (Fig. 4(b)), the lattice constant of the bcc phase (Fig. 4(c)) is approximately 2.9 Å. The precipitates are also shown lying along the grain boundary in Fig. 4(d). The findings of a bcc phase with very close lattice constant to pure Cr has been reported in previous works for CrMnFeCoNi Cantor alloy [24]. The bcc precipitates are seen to be rich in Cr and depleted in Mn, Fe and Ni as shown in STEM–EDX maps in Figs. 4(e)–4(h). The precipitates found are shown in Figs. 4(e)–4(i), where the structure of these precipitates is consistent with the bcc symmetry. We also found precipitates within the recrystallised grains in the samples.

The presence of the bcc phase was not detected in previous studies performed with a CrMnFeNi concentrated multicomponent alloy with similar composition to the present work [15]. The phase stability of $Fe_{27}Ni_{28}Mn_{27}Cr_{18}$ concentrated multicomponent alloy has been investigated by first principles DFT cluster expansion and Monte Carlo simulations [25]. The simulations predicted that Cr tetrahedral clusters in the fcc lattice are not thermodynamically favoured and Cr segregation may precipitate into the bcc lattice, which is the ground state of pure Cr. The equimolar CrFeMnNi alloy has been predicted to be two phase (fcc+bcc) from solidification and stable in the temperature range T> 1000 K and at lower temperatures two phase (fcc+σ). After annealing at 1273 K for 6 days, the equimolar CrFeMnNi was found to contain three phases: fcc, bcc, and σ. In particular, the concentration and lattice spacing of the bcc phase was predicted by CALPHAD calculation and measured by XRD and EDS–SEM to reveal a Cr concentration in the range 44.2–45.2 at. %, and a lattice spacing of 0.28 nm [26].

3.2. Microstructural characterisation after irradiation

The Cr-rich BCC particles were also observed in the irradiated specimens (see Figs. 5(a) to 5(f)). These precipitates are most likely

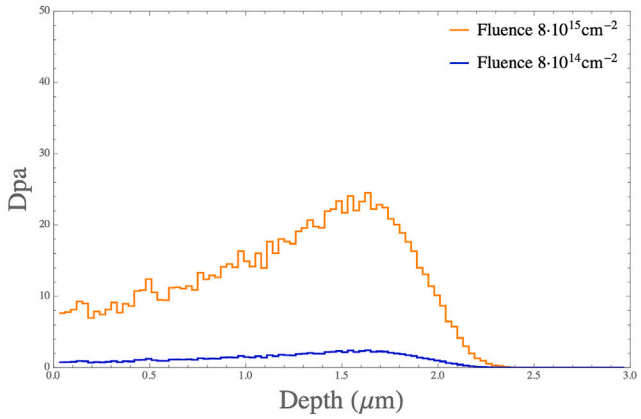

(a)

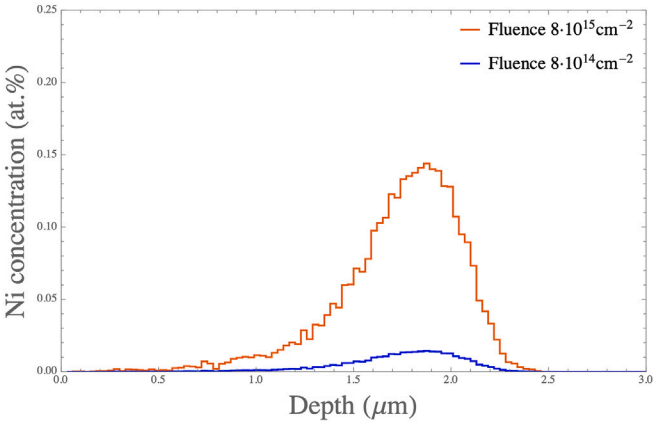

(b)

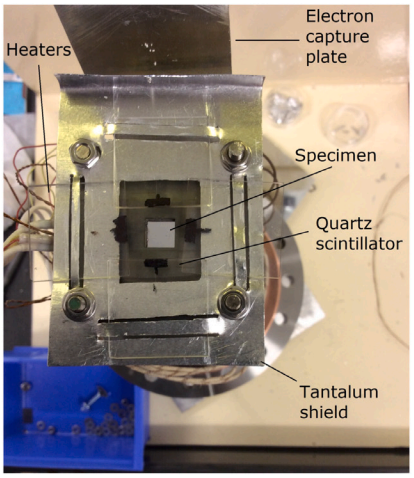

(c)

Fig. 3. Displacement per atom (Dpa) (a) and Nickel (atomic %) implantation profile (b) in $Fe_{28}Ni_{28}Mn_{26}Cr_{18}$ for the two fluences considered in Table 2 calculated with SRIM [19]. (c) Sample set up for irradiation experiment at beamline of Dalton Cumbrian Facility. An approximate area of 7 by 7 mm^2 delimited by scintillator quartz crystal is irradiated uniformly by the ion beam. The irradiation temperature is controlled by the heaters below the specimen and a chiller circulating continuously. The tantalum shield prevents the structural material of the stage from becoming activated by the incident radiation.

consistent with the BCC phase identified. An oxide phase, also rich in Cr and other elements such as Mn can also be distinguished from the same figure. It is likely that this phase is a spinel phase that was also observed in the un-irradiated specimens. The effect of irradiation in the volume fraction of the precipitates was not ascertained in this study, owing to the difficulties associated with making meaningful volume fraction measurements in the irradiated layer. The role that irradiation plays in these precipitates requires alternative techniques to the FIB used here to sample more irradiated volume and therefore get meaningful precipitate statistics. The findings of the Cr-rich BCC particles in the irradiated condition is in contrast to previously reported work in this alloy [15], which found no precipitates at all.

We also observed a NiMn segregated region in the irradiated samples with STEM–EDX maps in the irradiated specimens, but it was not possible to confidently rule out that these formed earlier in the thermo-mechanical processing stage before irradiation. These are shown in Figs. 5(c)–5(d). The dimensions of these fine precipitates made it difficult to identify the structure and lattice spacing by selected area diffraction in the TEM. The presence of an $L1_0$ NiMn phase after ageing at intermediate temperatures has been reported before in similar alloys [24,27].

The Bragg peak corresponding to the Ni irradiation was found at the approximate depth of 1.6 μm from SRIM simulations, which according to our estimations from Fig. 3 is separated from the Ni implantation peak which is at 1.9 μm (see Fig. 3). The implanted ion irradiated layer is observed with cross-section TEM micrographs in Figs. 8(a) to 8(f). The approximate depth of the layer measured between 1.9 and 2.1 μm is consistent with the predictions from SRIM simulations.

Recently, DFT(Density Functional Theory) based cluster expansion and Monte Carlo simulations published by the author have predicted the formation of $L1_0$ MnNi phase in $Fe_{27}Ni_{28}Mn_{27}Cr_{18}$ [25,28] at temperatures T<1300 K. Furthermore, simulations for formation $L1_2$ $CrFe_3$ in the temperature range 500–1200 K were also predicted by the author simulations, however the experimental measurements in this work did not indicate the presence of $L1_2$ $CrFe_3$.

In this work, and in agreement with self-ion irradiated studies in a similar composition multicomponent alloy, we found dislocation loops and no voids. In Figs. 8(c)–8(d), we show dislocation loop contrast corresponding to loops by using a two-beam condition (**g** = 220). The loop size for the specimens irradiated to 2 and 20 dpa at 450 C is found to be 10.6 nm and 13.7 nm with standard deviation of 8 nm and 33 nm respectively (see damaged regions of 1.4×1.8 μm^2 and 2.9×0.5 μm^2 for 2 and 20 dpa at 450 °C specimens in Fig. 7 respectively), the areal density of the loops for the same samples were found to be $2.9 \cdot 10^{10}$ cm^{-2} and $7.5 \cdot 10^{9}$ cm^{-2} for the 2 and 20 dpa specimens at 450 °C respectively. A high resolution image of the 20 dpa specimen irradiated at 450 °C showing the dislocation loops is given in Fig. 6. From the estimates of loop size and density it appears that the mean

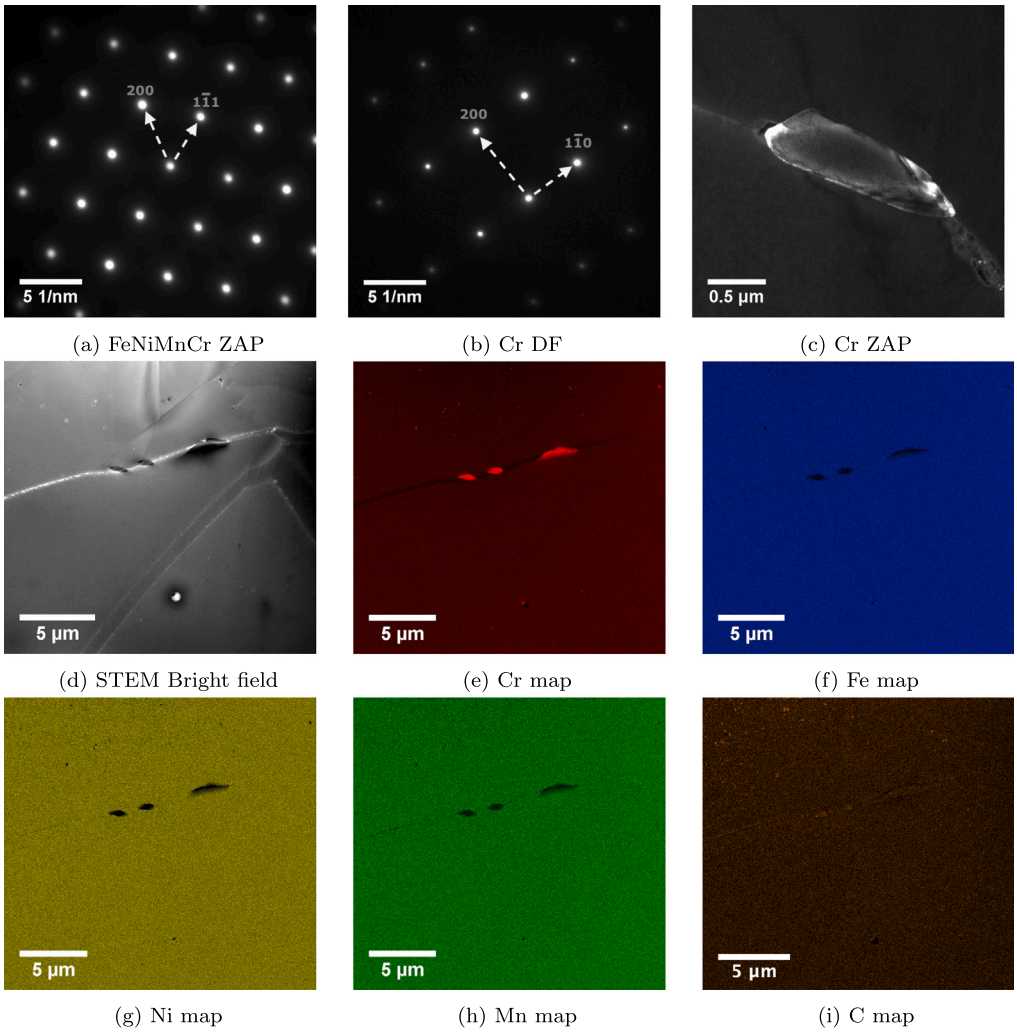

(a) FeNiMnCr ZAP (b) Cr DF (c) Cr ZAP

(d) STEM Bright field (e) Cr map (f) Fe map

(g) Ni map (h) Mn map (i) C map

Fig. 4. TEM selected area diffraction (the zone axis is [011] crystallographic direction for bcc phases (b), Dark Field Micrographs (c) and fcc phase (a). TEM selected area diffraction (the zone axis is [011] crystallographic direction for the fcc matrix). STEM Bright Field (d), and STEM energy dispersive X-ray maps of Cr (e), Fe (f), Mn (h), Ni (g), and C (i).

loop size increased with temperature of irradiation, and that the loop density decreased. For further quantitative analysis of the irradiation effects we find that due to the standard deviation in the present work being large limits possible correlation studies between loop size and effect of irradiation in the mechanical properties. For this purpose we will discuss another technique to quantify the mechanical properties in the following section. In fcc materials, the vacancies and interstitials are known to form dislocation loops of vacancy or interstitial types as well as voids. In situations where vacancy mobility is low due to an operating temperature less than approximately half of the melting temperature, vacancy dislocation loops are known [29] to be unstable and collapse due to the higher capture radius of dislocation for interstitial than vacancy point defects. Thus resulting in the annihilation of vacancy loops by diffusing interstitial point defects and leaving the only interstitial loops stable. Based on the dislocation bias argument we expect that the loops are of interstitial-type. Voids and dislocation loops were found in pure Ni after self-ion irradiations at doses as high as 13 dpa and temperatures 300–725 °C [30]. Westmore et al. reported significant difficulties in measuring the dislocation loop densities due to the their dense distribution. They estimated diameters ranging between 44 and 95 Å, and number densities $3.0 \cdot 10^8 - 7.8 \cdot 10^{10}$ cm^{-2}.

Preparation of TEM lamellae using Ga ions with the FIB technique can produce ripple-shaped contrast and black dot contrast [31]. A comparison of the un-irradiated and irradiated specimens shown in Figs. 8(a)–8(b) and 8(c)–8(d) demonstrates that the damage seen is not a result of FIB preparation; there is no damaged layer in the un-irradiated samples when compared to remaining irradiated samples Figs. 8(c)–(f). The dislocation loops may therefore be attributed to the Ni 5 MeV irradiation field and not from the FIB preparation work. The observed damaged layer in the irradiated sample in Fig. 8(d) has a varying depth between 1.9 and 2.1 µm is consistent with SRIM 5 MeV Ni implantation and dpa simulations as shown in Figs. 3 and 3.

3.3. Irradiation hardening from depth-sensing nanoindentation tests

Bulk equivalent hardness in irradiated specimens, H_0, was computed from fitting the contact depth-dependent hardness $P[h_c]/A_c[h_c]$. The hardness plots are shown in Fig. 9(a) and (b). Several models for irradiation hardening have been reported in the literature [32], the simplest one being Kasada two parameter model [33]. The hardness–contact depth plots were fitted to Kasada's film/substrate model in terms of parameters h_0 and H_0 similar to the Nix–Gao indentation size effect (ISE) [34], $H[h_c] = H_0\sqrt{1 + h_0/h_c}$. The shoulder (change in tangent in the $H^2 - 1/h_c$ plot) in the hardness envelope plots of the irradiated samples can be observed from Figs. 9(a) and (b). The inflection points in (0.2, 20 dpa for 450C and 2, 20 dpa for 300C) are approximately located at 200 nm. We use the inflection point for the upper end for fitting of the data to Kasada's model, $H[h_c] = H_0\sqrt{1 + h_0/h_c}$, which

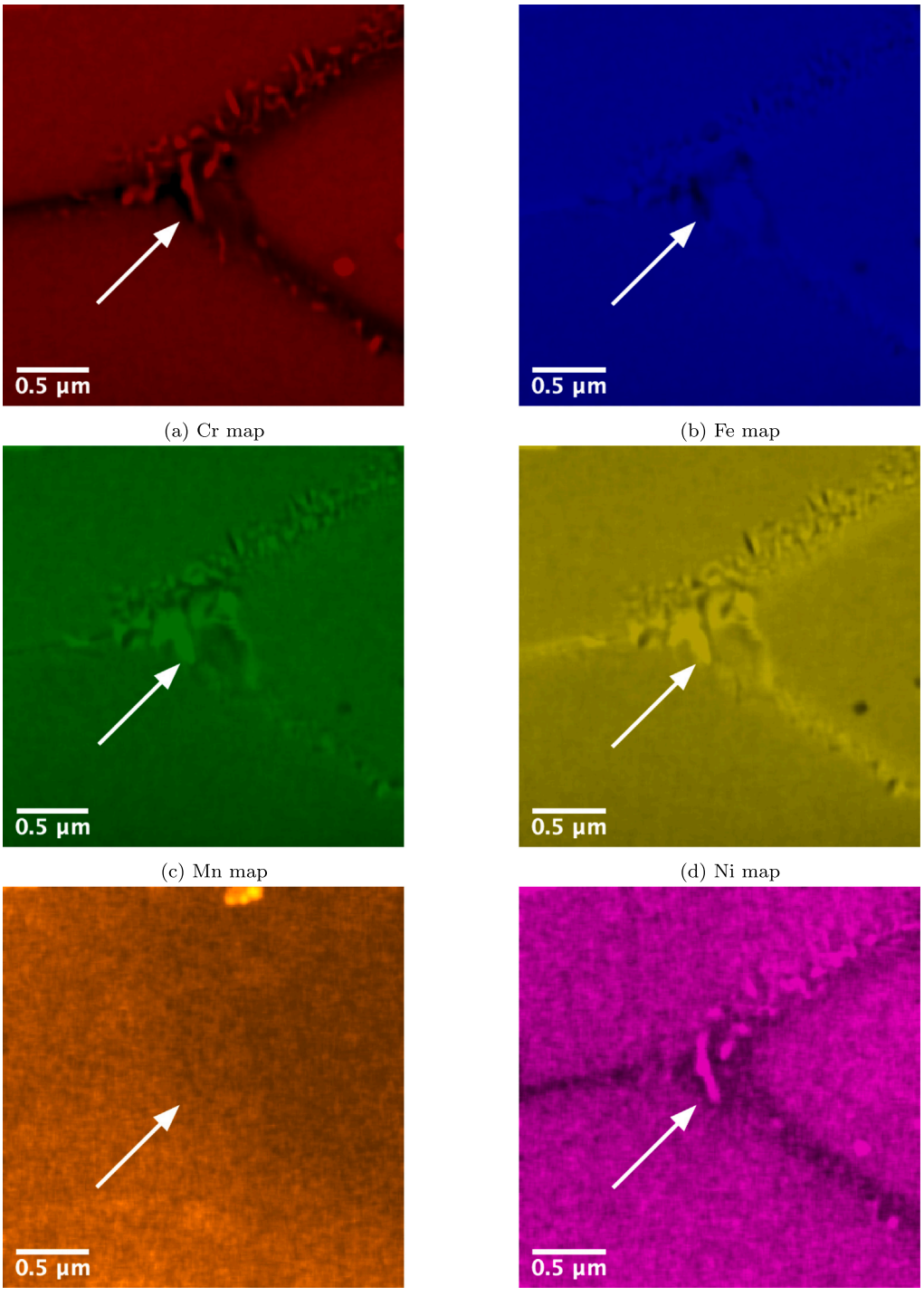

(a) Cr map (b) Fe map

(c) Mn map (d) Ni map

(e) C map (f) O map

Fig. 5. STEM EDX maps of Cr, Fe, Mn, Ni, C, and O at a triple junction. The arrow points to the NiMn phase.

was approximately given by $3 < 1/h_c < 10$ µm^{-1} for all the samples (see Fig. 9(c)–(d)). The range chosen for the h_c is consistent with a plastic zone radius caused by the indenter of 0.7 and 2.4 µm which are approximately equal or less than the depth of the irradiation damaged layer of 2.25 µm. The estimates of the plastic zone radius were obtained with Chen–Bull model developed for coated substrates [35]. Note that this range for data fitting is approximately consistent with similar ion-irradiated specimens [33,36], and that the hardness squared curve for the non-irradiated curve in the corresponding range fits to a straight line (see 9(e)) as in Nix–Gao model. The dashed lines in Figs. 9(c) and (d) correspond to the fitting of the data to Kasada's film/substrate model. The intercept of this lines with the vertical axis determines H_0^{irr}. The curve for 2 dpa at 450 °C is not really showing the inflection point. This could be a material issue or an irradiation issue. Bulk equivalent irradiation hardening in the damaged layer of self-ion implantation is then estimated by subtracting the equivalent bulk hardness of the un-irradiated specimens from the each of the bulk-equivalent hardness in the irradiated samples i.e. $\Delta H_{irr} = H_0^{irr} - H_0^{nonirr}$. These irradiation hardening quantities are obtained from the fits in Fig. 9(c)–(d) and the

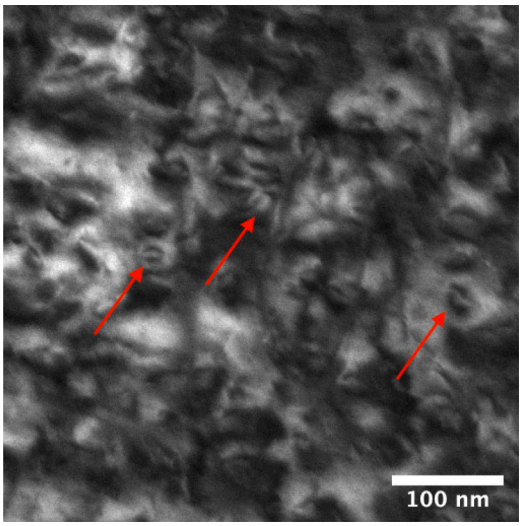

Fig. 6. Dislocation loops in the sample irradiated to 20 dpa at 450 °C.

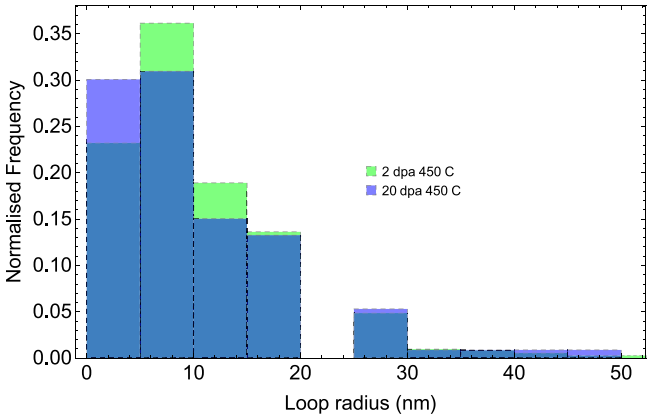

Fig. 7. Histogram of loop radius for the specimen irradiated to 2 and 20 dpa at temperature 450 °C.

numerical values are indicated in Table 3 as a function of dose and irradiation temperature.

The bulk equivalent hardness H_0^{irr} can be qualitatively interpreted within the volume fraction model in the approximation of half-sphere plastic zone of radius R_{pz} [32,37]:

$$H_0^{irr} = \frac{3}{2R_{pz}} \int_0^{R_{pz}} \left(1 - \frac{z^2}{R_{pz}^2}\right) H_0(z) dz \quad (1)$$

where $H_0(z)$ is assumed to be formed by a constant term (homogeneous bulk hardness as in the Nix–Gao model) and a dose-dependent hardening term given by a power law function of the dpa profile

$$H_0(z) = H_s + \chi(\mathrm{dpa}(z))^p \quad (2)$$

A modified Nix–Gao model with irradiation effect is obtained by using the volume fraction model expression for H_0^{irr} [32,37]

$$H_{irr} = H_0^{irr} \sqrt{1 + \frac{h^*}{h}} \quad (3)$$

This last expression has the same functional form as Kasada's model used in the following results when evaluated at a given contact depth.

From the irradiation hardening $\Delta H_{irr} = H_0^{irr} - H_0^{nonirr}$ for each of the irradiated samples in Table 3 we find that hardness increases with dose up to 4 GPa at all irradiation temperatures. Furthermore we find that irradiation temperature effects from 300 and 450 °C resulted in no significant change in the irradiation hardening. We calculated the experimental hardness increase due to irradiation by an alternative approach consisting on evaluating the hardness at the specific depth were the transition occurs between the near-surface damage and the undamaged substrate [15,34]. The data obtained compares well with the predictions from Kasada's fitting outlined above. For completion we have added these estimated hardness increments from the alternative approach to Table 3. Furthermore, we estimate from the number density of loops and their area an increase in hardness of 1.3 and 1.5 GPa for the samples irradiated at 2 dpa and 20 dpa at 450 C respectively. The discrepancy between the estimate hardness increases of Kasada's model and the estimate from the dislocation loops could be due to difficulties in counting the dislocation loops.

Kumar et al. [15] reported room temperature and 500 °C depth-sensing nanoindentation results in ion-irradiated CrMnFeNi. We have compared their data to ours in Table 3. In this work, we explored high doses to 20 dpa, and find that the increase in hardness after irradiation at 450 °C is 4.4 GPa, which expands the knowledge of the irradiation behaviour of this alloy after the hardness increase value of 0.47 GPa reported in [15] after 3 dpa of irradiation. The error bar magnitude difference for the low dose data at 300 °C of 0.9 is attributed to scatter and difficulty to fit the data. The remaining samples showed less scatter in the data, and the error bar could be reduced to less than 0.7 GPa.

Self-ion irradiation in Ni has primarily been focused on void swelling [30], and to the best of our knowledge there are no data for hardening from dislocation loops in pure nickel. Recently, Voyevodin et al. performed 1.4 MeV Ar ion irradiations in a multicomponent CrFeMnNi alloy (with composition 20, 40, 20, 20 $wt.\%$ respectively) to investigate the radiation behaviour by nanoindentation [36]. They have shown that the increasing in hardness measured from continuous stiffness depth-sensing nanoindentation followed by fitting to Kasada method [33] in the CrFeMnNi were 0.75, 1.0 , and 1.25 GPa after 0.3, 1 and 5 dpa of Ar ion irradiations. Their hardness of 0.75 GPa at 0.2 dpa compares reasonably well with out measurement of 0.5 GPa at 0.5 dpa; on the other hand our measurement of 2.5 GPa at 2 dpa is found to be higher than the 1 GPa hardness reported at 1 dpa. The difference could be attributed to the different ion used in the irradiation experiment or by the exact composition of the alloy.

The effect of Cr-rich precipitates dispersed in the matrix of CrMnFeNi concentrated multicomponent alloy is expected to contribute to work hardening when compared to the precipitate free condition approximately as the square root of the precipitate volume fraction. The powder diffraction limiting resolution is estimated to 5% volume fraction. Our XRD analysis could not detect the presence of the Cr-rich precipitate particles in the concentrated multicomponent alloys (Fig. 2), and the TEM analysis could evaluate the presence of not more than 1 or 2 Cr-rich precipitates overall (Fig. 4(c)). Therefore the expected contribution to work hardening in CrMnFeNi concentrated multicomponent alloy by the Cr-rich precipitates cannot be estimated with any confidence in this case. A more accurate evaluation of the role of irradiation in the precipitate volume fraction would require alternative techniques in addition to XRD, and TEM.

4. Conclusion

In the un-irradiated condition, we find Cr-rich bcc precipitates in the fcc-$Fe_{28}Ni_{28}Mn_{26}Cr_{18}$ concentrated multicomponent alloy matrix, in contrast to previously reported work in this alloy [15], which found no precipitates in any condition. In the irradiated state we find that dislocation loops of interstitial-type occur under irradiation, but in very high number densities making quantitative analysis difficult. To understand the implications of these radiation-induced defects in concentrated multicomponent alloys we use a hardening model based on previous work to convert measured depth-sensing nanoindentation hardness in the damaged layer to bulk equivalent hardness. Change in hardness is measured at 0.2, 2, and 20 dpa and at irradiation temperatures of

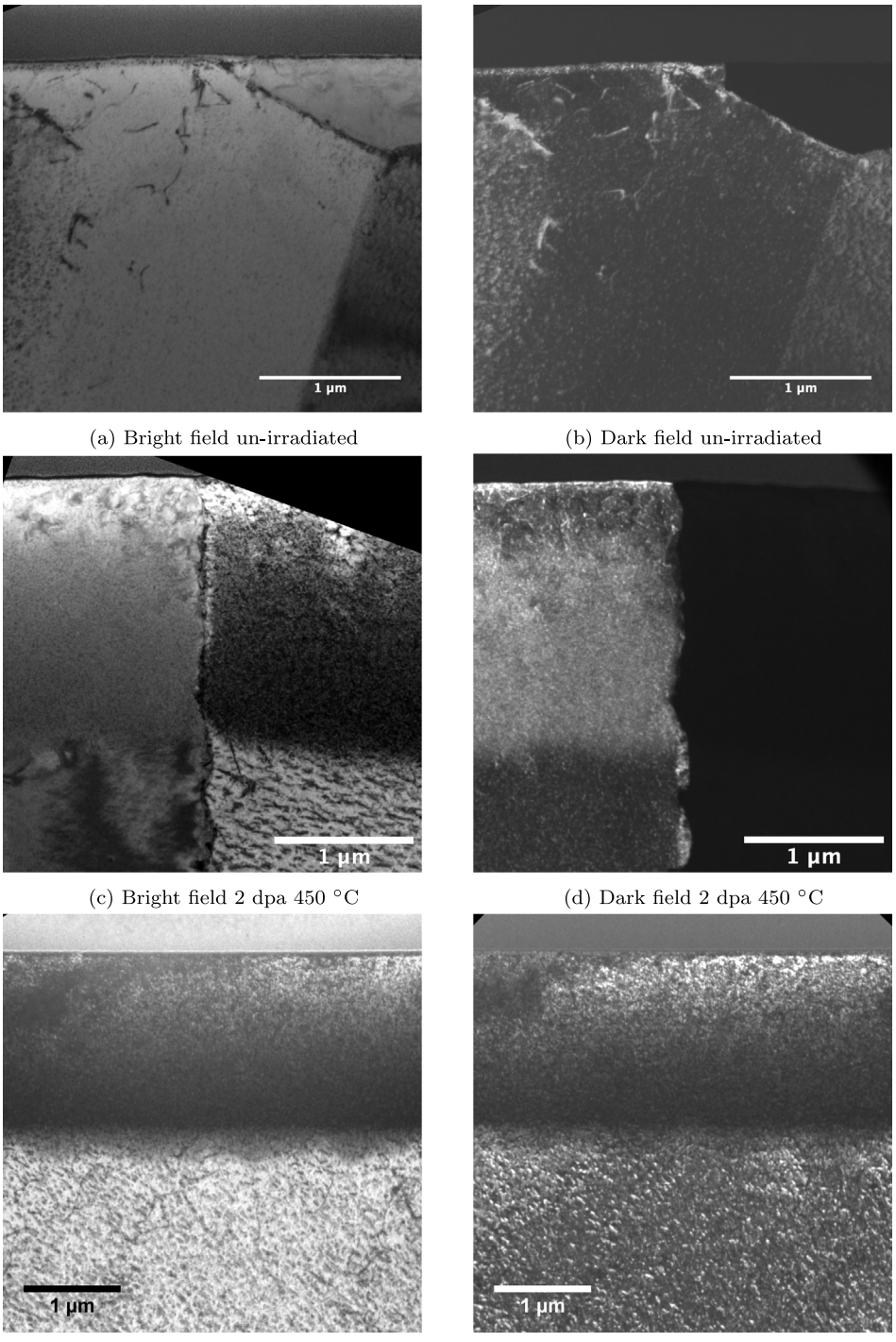

(a) Bright field un-irradiated (b) Dark field un-irradiated

(c) Bright field 2 dpa 450 °C (d) Dark field 2 dpa 450 °C

(e) Bright field 20 dpa 450 °C (f) Dark field 20 dpa 450°C

Fig. 8. Micrographs of un-irradiated (a)–(b) and irradiated concentrated multicomponent alloys lamela prepared by the FIB lift-out method (c)–(f). In the lamellae, the platinum layer of protection is found at the top of the images. The platinum location indicates the entry direction of the ion irradiation as it penetrated the bulk of the recrystallised specimen. In Fig. (c) the half grain in the top left corner is cut off due to the image rotation in the TEM.

300 °C and 450 °C. The findings of this work suggest that irradiation hardening at 20 dpa is as high as 4 GPa. As a conclusion, it is found that at high doses, the effect of irradiation hardening is significant in the CrFeMnNi multicomponent concentrated alloy, and the alloy is not stable to precipitation of secondary Cr-rich bcc phase.

CRediT authorship contribution statement

A. Fernández-Caballero: Conceptualization, Methodology, Software, Formal analysis, Writing - original draft, Writing - review & editing, Investigation, Visualization, Funding acquisition. **E. Bousser:** Methodology, Software, Investigation, Formal analysis, Writing - review & editing. **S.M. Shubeita:** Methodology. **P.T. Wady:** Methdology. **Y. Gu:** Methodology. **Ram Krishna:** Methodology. **M.J. Gorley:**

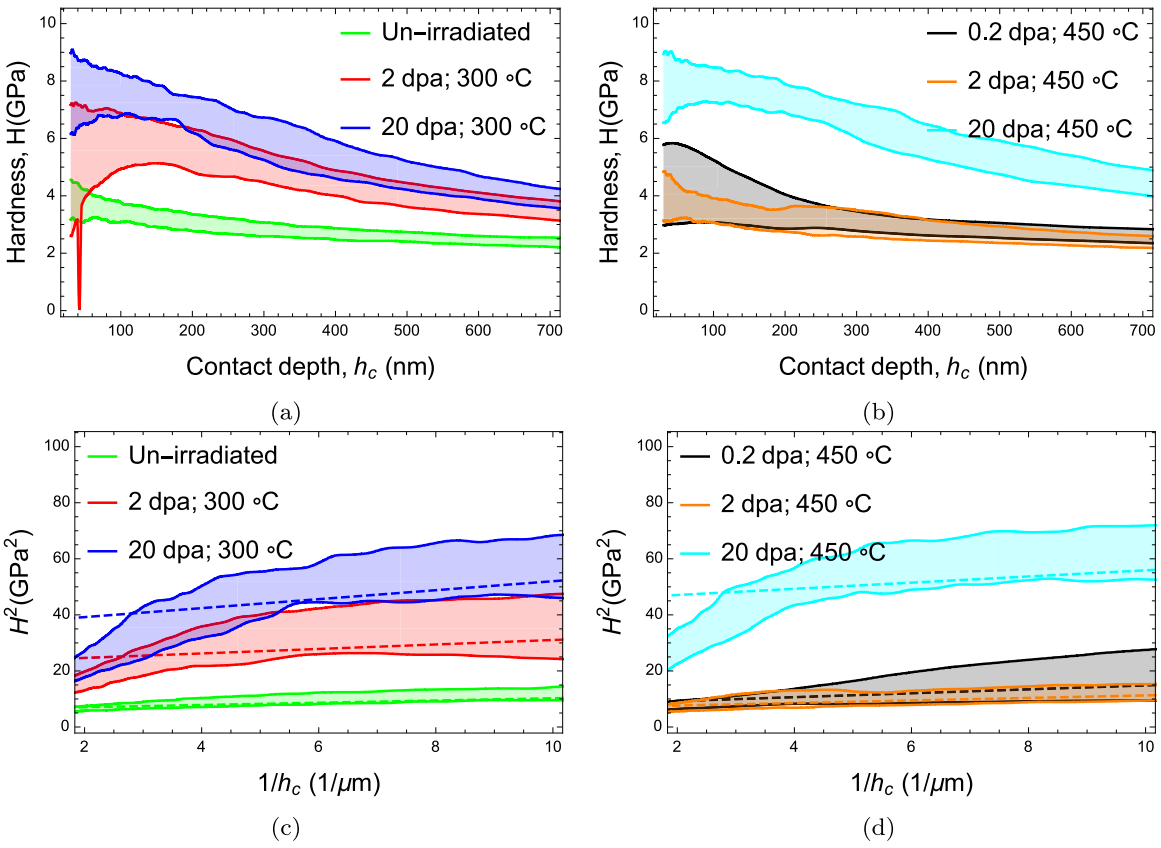

Fig. 9. Hardness and hardness squared envelope plots, (a)–b) and (c)–(d) respectively. The envelope is a consequence of the statistical spread from 25 indentations and CSM data per sample/condition.

Table 3
Irradiation hardening (in GPa units) concerning non-irradiate condition as obtained from this work (first two rows), and previous work [15] (last two columns). The un-irradiated samples had a reference hardness of 2.6 ± 0.2 GPa.

Irradiation temperature (Kasada's) (°C)	Low dose (0.2 dpa)	Medium dose (2 dpa)	High dose (20 dpa)
300		2.5 ± 0.9	3.7 ± 0.4
450	0.5 ± 0.5	0.3 ± 0.2	4.4 ± 0.7
Irradiation temperature (experimental) (°C)	Low dose (0.2 dpa)	Medium dose (2 dpa)	High dose (20 dpa)
300		2.71	4.14
450	0.54	0.11	4.44
Irradiation Temperature ([15])	Low dose (0.3 dpa)	Medium dose (3 dpa)	
25	2.31		
500	0.33	0.47	

Conceptualization, Funding acquisition, Writing - review & editing, Supervision. **D. Nguyen-Manh:** Conceptualization, Supervision. **P.M. Mummery:** Conceptualization, Funding acquisition, Writing - review & editing, Supervision. **E.J. Pickering:** Conceptualization, Investigation, Visualization, Writing - review & editing, Supervision.

Declaration of competing interest

The authors declare that they have no known competing financial interests or personal relationships that could have appeared to influence the work reported in this paper.

Acknowledgements

A.F.-C. thanks Russell Goodall from Sheffield University for the production of the samples at the University of Sheffield. A.F.-C. acknowledges assistance with the sample irradiation process to Paul Wady (Dalton Cumbrian Facility, The University of Manchester), and Octav Ciuca (Department of Materials, The University of Manchester). This research was funded by the Euratom research and training programme, UK 2014–2019 under Grant Agreement No. 633053 and by the Research Council UK (RCUK) Energy Programme (Grant Number EP/P012450/1). The views and opinions expressed herein do not necessarily reflect those of the European Commission. A.F.-C. was funded by the EPSRC, UK grant (EP/L01680X/1) through the Materials for Demanding Environments Center for Doctoral Training.

References

[1] J.W. Yeh, S.K. Chen, S.J. Lin, J.Y. Gan, T.S. Chin, T.T. Shun, C.H. Tsau, S.Y. Chang, Nanostructured high-entropy alloys with multiple principal elements: Novel alloy design concepts and outcomes, Adv. Energy Mater. 6 (5) (2004) 299–303.

[2] M.C. Troparevsky, J.R. Morris, M. Daene, Y. Wang, A.R. Lupini, G.M. Stocks, Beyond atomic sizes and Hume–Rothery rules: Understanding and predicting high-entropy alloys, JOM 67 (10) (2015) 2350–2363.

[3] B. Cantor, I. Chang, P. Knight, A. Vincent, Microstructural development in equiatomic multicomponent alloys, Mater. Sci. Eng. A 375–377 (2004) 213–218.

[4] Y. Zhang, T.T. Zuo, Z. Tang, M.C. Gao, K.a. Dahmen, P.K. Liaw, Z.P. Lu, Microstructures and properties of high-entropy alloys, Prog. Mater. Sci. 61 (October 2013) (2014) 1–93.

[5] S. Zinkle, G. Was, Materials challenges in nuclear energy, Acta Mater. 61 (3) (2013) 735–758.

[6] D. Stork, S. Zinkle, Introduction to the special issue on the technical status of materials for a fusion reactor, Nucl. Fusion 57 (9) (2017) 092001.

[7] C. Lu, L. Niu, N. Chen, K. Jin, T. Yang, P. Xiu, Y. Zhang, F. Gao, H. Bei, S. Shi, M.-R. He, I.M. Robertson, W.J. Weber, L. Wang, Enhancing radiation tolerance by controlling defect mobility and migration pathways in multicomponent single-phase alloys, Nature Commun. 7 (2016) 13564.
[8] T. Egami, W. Guo, P.D. Rack, T. Nagase, Irradiation resistance of multicomponent alloys, Metall. Mater. Trans. A 45 (1) (2014) 180–183.
[9] T. Egami, M. Ojha, O. Khorgolkhuu, D.M. Nicholson, G.M. Stocks, Local electronic effects and irradiation resistance in high-entropy alloys, Jom 67 (10) (2015) 2345–2349.
[10] A. Fernandez-Caballero, Radiation Behaviour of High-Entropy Alloys for Fusion Reactor Environments (Ph.D. thesis), Centre for Doctoral Training Materials for Demanding Environments, Faculty of Science and Engineering, The University of Manchester, 2019.
[11] E.J. Pickering, N.G. Jones, High-entropy alloys: A critical assessment of their founding principles and future prospects, Int. Mater. Rev. 61 (3) (2016) 183–202.
[12] N.D. Stepanov, D.G. Shaysultanov, M.A. Tikhonovsky, G.A. Salishchev, Tensile properties of the Cr–Fe–Ni–Mn non-equiatomic multicomponent alloys with different Cr contents, Mater. Des. 87 (2015) 60–65.
[13] Z. Wu, H. Bei, Microstructures and mechanical properties of compositionally complex Co-free FeNiMnCr 18 FCC solid solution alloy, Mater. Sci. Eng. A 640 (2015) 217–224.
[14] E. Bloom, R. Conn, J. Davis, R. Gold, R. Little, K. Schultz, D. Smith, F. Wiffen, Low activation materials for fusion applications, J. Nucl. Mater. 122 (1–3) (1984) 17–26.
[15] N.K. Kumar, C. Li, K. Leonard, H. Bei, S. Zinkle, Microstructural stability and mechanical behavior of FeNiMnCr high entropy alloy under ion irradiation, Acta Mater. 113 (2016) 230–244.
[16] C. Abromeit, Aspects of simulation of neutron damage by ion irradiation, J. Nucl. Mater. 216 (1994) 78–96.
[17] B. Toby, Program CMPR, version 1.34, NIST, 2005.
[18] P. Wady, A. Draude, S. Shubeita, A. Smith, N. Mason, S. Pimblott, E. Jimenez-Melero, Accelerated radiation damage test facility using a 5MV tandem ion accelerator, Nucl. Instrum. Methods Phys. Res. A 806 (2016) 109–116.
[19] J.F. Ziegler, M. Ziegler, J. Biersack, SRIM – the stopping and range of ions in matter (2010), Nucl. Instrum. Methods Phys. Res. B 268 (11–12) (2010) 1818–1823.
[20] R. Stoller, M. Toloczko, G. Was, A. Certain, S. Dwaraknath, F. Garner, On the use of SRIM for computing radiation damage exposure, Nucl. Instrum. Methods Phys. Res. B 310 (2013) 75–80.
[21] W. Oliver, G. Pharr, An improved technique for determining hardness and elastic modulus using load and displacement sensing indentation experiments, J. Mater. Res. 7 (06) (1992) 1564–1583.
[22] J. Schindelin, I. Arganda-Carreras, E. Frise, V. Kaynig, M. Longair, T. Pietzsch, S. Preibisch, C. Rueden, S. Saalfeld, B. Schmid, J.-Y. Tinevez, D.J. White, V. Hartenstein, K. Eliceiri, P. Tomancak, A. Cardona, Fiji: An open-source platform for biological-image analysis, Nature Methods 9 (7) (2012) 676–682.
[23] F. Otto, Y. Yang, H. Bei, E. George, Relative effects of enthalpy and entropy on the phase stability of equiatomic high-entropy alloys, Acta Mater. 61 (7) (2013) 2628–2638.
[24] F. Otto, A. Dlouhý, K.G. Pradeep, M. Kuběnová, D. Raabe, G. Eggeler, E.P. George, Decomposition of the single-phase high-entropy alloy CrMnFeCoNi after prolonged anneals at intermediate temperatures, Acta Mater. 112 (2016) 40–52.
[25] A. Fernández-Caballero, M. Fedorov, J. Wróbel, P. Mummery, D. Nguyen-Manh, Configurational entropy in multicomponent alloys: Matrix formulation from ab initio based hamiltonian and application to the FCC Cr–Fe–Mn–Ni system, Entropy 21 (1) (2019) 68.
[26] G. Bracq, M. Laurent-Brocq, L. Perrière, R. Pirès, J.M. Joubert, I. Guillot, The fcc solid solution stability in the Co–Cr–Fe–Mn–Ni multi-component system, Acta Mater. 128 (2017) 327–336.
[27] M.E. Bloomfield, K.A. Christofidou, N.G. Jones, Effect of Co on the phase stability of CrMnFeCoxNi high entropy alloys following long-duration exposures at intermediate temperatures, Intermetallics 114 (July) (2019).
[28] M. Fedorov, J.S. Wróbel, A. Fernández-Caballero, K.J. Kurzydłowski, D. Nguyen-Manh, Phase stability and magnetic properties in fcc Fe–Cr–Mn–Ni alloys from first-principles modeling, Phys. Rev. B 101 (2020) 174416.
[29] D. Olander, Fundamental Aspects of Nuclear Reactor Fuel Elements, Technical Information Center, U.S. Department of Energy, 1976.
[30] J.E. Westmoreland, J.A. Sprague, F.A. Smidt, P.R. Malmberg, Dose rate effects in nickel ion irradiated nickel, Radiat. Eff. 26 (1–2) (1975) 1–16.
[31] H.-H. Jin, C. Shin, J. Kwon, Fabrication of a TEM sample of ion-irradiated material using focused ion beam microprocessing and low-energy Ar ion milling, J. Electron Microsc. 59 (6) (2010) 463–468.
[32] X. Xiao, L. Yu, Nano-indentation of ion-irradiated nuclear structural materials: a review, Nuclear Materials and Energy 22 (September 2019) (2020) 100721.
[33] R. Kasada, Y. Takayama, K. Yabuuchi, A. Kimura, A new approach to evaluate irradiation hardening of ion-irradiated ferritic alloys by nano-indentation techniques, Fusion Eng. Des. 86 (9–11) (2011) 2658–2661.
[34] W.D. Nix, H. Gao, Indentation size effects in crystalline materials: A law for strain gradient plasticity, J. Mech. Phys. Solids 46 (3) (1998) 41–425.
[35] J. Chen, S.J. Bull, On the relationship between plastic zone radius and maximum depth during nanoindentation, Surf. Coat. Technol. 201 (7) (2006) 4289–4293.
[36] V.N. Voyevodin, S.A. Karpov, G.D. Tolstolutskaya, M.A. Tikhonovsky, A.N. Velikodnyi, I.E. Kopanets, G.N. Tolmachova, A.S. Kalchenko, R.L. Vasilenko, I.V. Kolodiy, Effect of irradiation on microstructure and hardening of Cr–Fe–Ni–Mn high-entropy alloy and its strengthened version, Phil. Mag. 100 (7) (2020) 822–836.
[37] F. Röder, C. Heintze, S. Pecko, S. Akhmadaliev, F. Bergner, A. Ulbricht, E. Altstadt, Nanoindentation of ion-irradiated reactor pressure vessel steels – model-based interpretation and comparison with neutron irradiation, Phil. Mag. 98 (11) (2018) 911–933.